Nanoscale

Design of super-strong and thermally stable nanotwinned Al alloys via solute synergy

Journal:	*Nanoscale*
Manuscript ID	NR-ART-08-2020-005707.R1
Article Type:	Paper
Date Submitted by the Author:	13-Sep-2020
Complete List of Authors:	Zhang, Yifan; Purdue univsersity, School of Materials Engineering Su, Ruizhe; Purdue University, Materials Engineering Xie, Dongyue; University of Nebraska-Lincoln, Mechanical and Materials Engineering Niu, Tongjun; Purdue University xue, sichuang ; Purdue University System, MSE Li, Qiang; Purdue University, Materials engineering Shang, Zhongxia; Purdue University, School of Materials Engineering Ding, Jie; Purdue univsersity, School of Materials Engineering Richter, Nicholas; Purdue University Wang, Jian; University of Nebraska-Lincoln Wang, Haiyan; Purdue University System, MSE; Neil Armstrong Engineering Building Zhang, Xinghang; Purdue University System, Materials Engineering

Design of super-strong and thermally stable nanotwinned Al alloys via solute synergy

Y.F. Zhang[a], R. Su[a], Dongyue Xie [c], T.J. Niu[a], S. Xue[a] Q. Li[a], Z. Shang[a], J. Ding[a], N.A. Richter[a], Jian Wang [c], H. Wang[a, b], X. Zhang*[a]*

[a] *School of Materials Engineering, Purdue University, West Lafayette, IN 47907, United States*

[b] *School of Electrical and Computer Engineering, Purdue University, West Lafayette, IN 47907*

[c] *Mechanical and Materials Engineering, University of Nebraska-Lincoln, Lincoln, NE 68588,*

**Corresponding author: X. Zhang, xzhang98@purdue.edu; Y.F. Zhang, zhan2592@purdue.edu;*

Abstract

Al alloys have widespread industrial applications. However, their mechanical strength is often much lower than steels. Here, we investigate the influence of solutes on achieving ultrahigh strength and thermal stability of nanotwinned Al alloys. *In situ* micropillar compression tests show the addition of a small number of Ti can significantly increase the mechanical strength of Al-Ni alloys to 2 GPa. Deformation induced detwinning, Ni segregation and grain coarsening as discovered in binary Al-Ni alloys are mostly absent in the ternary Al-Ni-Ti alloys. Moreover, the ternary Al-Ni-Ti alloys have outstanding thermal stability. Density function theory calculations reveal the synergetic pinning effect of Ni-Ti solute pairs on incoherent twin boundaries. This study demonstrates that the proper selection of synergistic solute pairs is critical to design the thermal stability and mechanical properties of nanotwinned Al alloys.

Key words: Nanotwins; Al alloys; high strength; thermal stability; density function theory.

1. Introduction

High-strength Al alloys have broad industrial applications. Extensive studies have focused on the processing and strengthening mechanisms of Al alloys. Precipitate strengthening is one common strengthening method in commercial Al alloys (AA2024, AA6061, AA7075). For example, aging treatment at 120 °C for 24 hours (T6 treatment) can introduce high-density precipitates in AA7075 alloy and leads to a maximum tensile strength of ~ 600 MPa [1,2]. Recently, Sun *et al* [3] revealed that room-temp cyclic loading can also induce precipitation strengthening in Al alloys.

Severe plastic deformation (SPD) techniques, including high pressure torsion (HPT) [4] and equal channel angular pressing (ECAP) [5], are promising to strengthen Al alloys. The SPD can refine grain size to several tens nanometers and introduce high-density dislocations as well as nanoprecipitates into Al alloys. So far, the strength limit of Al alloys processed by SPD is 1 GPa [6]. High-energy ball milling is another method to fabricate high strength nanocrystalline (NC) Al alloys, and has been extensively studied. Sasaki *et al* [7] reported the ball-milled Al-Fe alloys with 1 GPa compressive strength. Recently, Pun *et al* [8] fabricated Al-Mg alloys with 1 GPa flow stress through high-energy ball milling. Furthermore, high-energy ball milling can increase the solubility of Cr, Fe, Ti in Al [9].

Nanotwins can greatly improve the strength and ductility of Cu [10], stainless steel [11], Ni[12] and Ag [13] *etc*. Moreover, nanotwinned (NT) metals have shown superior thermal stability [14–16] and radiation resistance [17,18] compared with their coarse grained (CG) or NC counterparts. Molecular dynamic (MD) simulations [19] have confirmed that both coherent twin boundary (CTB) and incoherent twin boundary (ITB) [20] can effectively impede the dislocation transmission. However, twinning is difficult in Al because of its high stacking fault energy (SFE) of ~142

mJ/m^2 [21] and low energy barrier (< 10 mJ/m^2) for nucleation of trailing partials [22]. Conventional fabrication methods such as casting, or rolling are unlikely to introduce high-density twins into Al. Though twining has been reported in sputtered NC Al [23], the twin boundary density was insufficient to strengthen Al.

Recent studies have shown that the addition of Ti [24], Mg [25], Fe [26], Co [27] , and Ni [28] can introduce high-density twin boundaries into Al. The room temperature equilibrium solubility of these elements is very limited. However, the high cooling rate in magnetron sputtering (~10^6 - 10^7 K/s) can extend the solubility of solutes significantly in Al, resulting in supersaturated solid solution alloys [29]. The NT binary Al-Ni alloys, with nano grains (~ 5-100 nm) and supersaturated solutes, have an ultrahigh hardness of ~ 6 GPa and a flow stress of 1.7 GPa [28]. It is worth mentioning that the *3d* transition metals, such as Fe, Ni, and Co, are effective to refine grains and introduce nanotwins. Density function theory (DFT) calculations [27] and MD simulations [26] showed that the addition of these transition elements can decrease the SFE and increase the energy barrier of detwinning in Al. However, like most NC materials, these binary NT Al binary alloys have limited thermal stability because of the large fraction of grain boundaries (GBs) with higher excess free energies [30]. Also our previous studies revealed deformation induced grain coarsening and rotation in deformed NT Al-Ni [28], and Al-Co [27] alloys. It is necessary to improve the thermal stability of NT Al alloys for applications at elevated temperatures.

Studies have shown that the thermal stability of NC alloys can be enhanced through solute segregation [31,32] and the precipitation on GBs [33]. Solute segregation may decrease free energy of GBs [34], while precipitation can retard GB migration and grain coarsening through Zener pinning effect [35]. However, solute segregation and precipitation may lead to detwinning,

recrystallization and softening in NT Al alloys. It remains a challenge to improve the microstructure stability of super saturated Al solid solution alloys.

Here, we address this challenge via a solute synergy approach. We hypothesize that the selection of a third element may effectively improve the thermal and mechanical stability of binary NT Al-Ni alloy. To test our hypothesis, Ti has been selected to fabricate Al-Ni-Ti alloy by using magnetron sputtering. The selection of the Ti is based on properties such as *d-orbital* energy level [36], diffusivity in Al [36], bonding order with Al and Ni [37,38]. Our studies show that the addition of a small amount of Ti can indeed enhance the strength, deformation stability and thermal stability of Al alloys prominently. The findings of this work demonstrate the promising method to design high-strength and thermally stable Al alloys through solute synergy.

2. Experimental

At room temperature,1.6-μm-thick Al-Ni and Al-Ni-Ti films were deposited on HF-etched Si (111) substrates by direct current (DC) magnetron sputtering using high-purity Al (99.99%), Ni (99.99%), and Ti (99.99%) targets. Prior to depositions, the base pressure of the main chamber was ~ 8×10^{-9} torr. The argon gas pressure was maintained at ~ 3 mtorr during the deposition. X-ray diffraction (XRD) θ-2θ and pole figure scans were conducted on a Panalytical Empyrean X'pert PRO MRD diffractometer to evaluate the texture and microstructure of deposited Al-Ni and Al-Ni-Ti alloys. Subsequently, the chemical compositions of deposited alloys were examined using energy dispersive spectroscopy (EDS) on a Thermo Fisher Quanta 3D FEG scanning electron microscope. Transmission electron microscopy (TEM) analyses were performed on Thermo Fisher Talos 200X analytical microscope operated at 200 kV. Crystal orientation analyses were performed on NanoMegas ASTAR system installed on the Talos 200X

TEM microscope using nanobeam diffraction technique. The OIM software was used for ASTAR data analysis.

Hardness and elastic modulus of Al alloys were measured by a Bruker TI Premier nanoindenter at different indentation depths using displacement control mode. To ensure the reliability of data, at least 100 indents were conducted on each sample with indentation depth less than 15 % of the total film thickness (1.6 μm). Micropillars were fabricated using focused ion beam (FIB) technique. To avoid the buckling and deformation instability, diameters of these pillars were designed to be ~750 nm with a height-to-diameter aspect ratio of 2:1. A Bruker PI 88xR PicoIndenter equipped with a 5-μm diamond flat punch tip was used to perform *in situ* micropillar compression tests inside the Quanta 3D scanning electron microscopy (SEM) microscope, at a constant strain rate of 5×10^{-3} s^{-1}. After the compression experiments, the deformed pillars were cut and thinned by using FIB for post-compression TEM analyses. To minimize ion damage, 2 kV beam voltage was applied to the final polishing stage.

Al-Ni and Al-Ni-Ti alloys were annealed inside the AJA sputtering chamber with high vacuum (8×10^{-9} torr) at different temperatures for 1.5 h. After annealing, the samples were cooled to room temperature in the chamber at a cooling rate of ~15 °C/min. Then, hardness tests, systematic XRD and TEM analyses were performed on the annealed Al-Ni and Al-Ni-Ti alloys.

DFT calculations were performed to probe the effect of Ti solutes on the SFE and other energy states in Al. Vienna ab-initio simulation package (VASP) was used to conduct DFT calculations. During this calculation, projector augmented wave (PAW) method [39], Perdew-Burke-Ernzerhof (PBE) exchange-correlation density functional [40,41], and generalized gradient approximation (GGA) approach [42] were employed. For the pseudopotentials in this calculation, the electron configuration of Al, Ni, and Ti is $[Ne]3s^2 3p^1$, $[Ar]3d^8 4s^2$, and $[Ar]\ 3d^2 4s^2$ were

adopted. The kinetic energy cut-off for the plane wave expansion was set to 500 eV. The self-consistent iteration and atomic realization stopped with the criteria of 10^{-6} eV and 0.01eV/Å respectively.

3. Results

3.1 Microstructure characterization

Systematic microstructure characterizations were performed on Al-Ni and Al-Ni-Ti alloys. The Al-4.5 Ni and Al-4.5Ni-3Ti alloys were selected to demonstrate the influence of Ti on the microstructure of Al-Ni alloys. XRD patterns in Fig. 1(a) show that the addition of Ti solutes can promote the {111} texture of Al-4.5 Ni as evidenced by the absence of the Al (311) peak in the Al-4.5Ni-3Ti. XRD pole figure analysis further demonstrates the effect of Ti on improving the texture of Al-4.5Ni. The Al-4.5Ni-3Ti is highly-twinned with six-fold symmetrical diffraction spots belonging to matrix (black dash line) and twin (red dash line) (Fig. 1(c)), in comparison to the strong central spot and ring-like contour (indicating the {111} out-of-pane texture and significant in-plane rotation) in Al-4.5Ni (Fig. 1(b)). The hardnesses of Al-Ni-Ti, Al-Ni alloys and Al alloys from other studies [6,24,26,28,43,44] are plotted as a function of $d^{-1/2}$ in Fig. 1(e), where d is the average grain size. Hardnesses of binary and ternary alloys are also plotted versus the Ni composition as shown in Fig. 1(d). Evidently, the Al-Ni-Ti alloys have higher hardness than their Al-Ni alloys counterparts with similar Ni composition. Also, the sputtered Al-7.5Ni-3Ti has a high hardness of 6.8 ± 0.2 GPa, making it one of the strongest Al alloys reported to date.

TEM analysis were conducted on Al-Ni and Al-Ni-Ti alloys. Bright-field (BF) and dark-field (DF) XTEM images (Fig. 2, 3 (a-b)) reveal columnar grains in Al-4.5Ni and Al-4.5Ni-3Ti. The inserted selected area diffraction (SAD) pattern in Fig. 2(a) confirms the existence of twins

in the polycrystalline Al-4.5Ni alloy. The SAD pattern in Fig. 3(a) displays the highly twinned microstructure in the Al-4.5Ni-3Ti, consistent with the pole figure analysis. Grain size distribution statistics presented in Fig. 2(c) and Fig. 3(c) show an average grain size of 39 and 30 nm in the Al-4.5 Ni and Al-4.5Ni-3Ti, respectively. Fig. S1 shows the average grain size of Al-7.5Ni-3Ti is 8 nm.

High-resolution TEM (HRTEM) images (Fig. 2(d), Fig. 3(d)) show ITBs and 9R phases (broad ITBs) in Al-4.5Ni and Al-4.5Ni-3Ti. The statistics show the twin volume fraction in Al-4.5Ni-3Ti and Al-4.5Ni is 55% and 25%, respectively. Apart from these vertical ITBs and high-angle grain boundaries (HAGBs), a small number of vertical CTBs were also found in the Al-4.5 Ni (Fig. 2(e-g)). Because of the less grain rotation and better texture, low angle grain boundaries (LAGBs) (Fig. 3(f)) were dominant over HAGBs in the Al-4.5Ni-3Ti alloy. Another significant feature in Al-4.5Ni-3Ti is the high-density sub-column boundaries. As shown in Fig. 3(e), one column with 9R phases contains several sub-columnar boundaries, depicted by white dash lines. These sub-column boundaries are LAGBs with small misorientation angles (0.5 -1.5^{o}).

3.2 *In situ* micropillar compression

Fig. 4(a-j) are snapshots of *in situ* pillar compression videos showing the pillar morphology evolution of Al-4.5 Ni and Al-4.5Ni-3Ti at different stain levels. The morphologies of the undeformed pillars are delineated by white dash lines. As shown in Fig. 4(c), prominent local deformation emerged in Al-4.5 Ni when ε = 10% and ended up with significant dilations on pillar top indicated by red arrows. Dilations were less prominent for the Al-4.5Ni-3Ti. (Please see supplementary video 1-2 for more details)

True stress - strain curves of Al, Al-4.5Ni, and Al-4.5Ni-3Ti are compared in Fig. 4(k). The true stress was calculated using real-time diameter of the deformed pillars captured by the *in*

situ videos. In this study, the out-of-plane engineering strains have been used to evaluate the overall deformation of the pillar. As shown in Fig. S4 (a), the instantaneous diameters at the middle and top of Al-4.5Ni pillar were recorded to calculate the in-plane strains. Fig. S4(b) shows the out-of-plane and in-plane engineering strains of the Al-4.5Ni deformed pillar. If we consider the volume fraction of deformed top (~35 vol.%) and less deformed base (~ 65 vol.%), the out-of-plane strain can represent the average strain level for the deformed pillars.

The flow stress of Al-4.5Ni-3Ti, Al-4.5Ni, and monolithic Al at the ε of 10% is ~1.8 GPa, 1.0 GPa, and 0.25 GPa respectively. Work hardening rates ($d\sigma/d\varepsilon$) of Al-4.5Ni (blue dot lines) and Al-4.5Ni-3Ti (red dotted lines) were calculated and plotted with true stress-strain cures (solid lines) in Fig. 4(l). The Al-4.5Ni-3Ti exhibited significantly higher work hardening rate than the Al-4.5Ni when $\varepsilon < 8\%$.

3.3 Post-compression analysis

TEM analyses were performed to examine the microstructure, orientation and chemical composition of the deformed Al-4.5 Ni (Fig.5) and Al-4.5Ni-3Ti (Fig. 6) pillars. Fig. 5(a-b) show distinct microstructures at different locations of the deformed Al-4.5Ni pillar. Nanocolumns with 9R phases were found in the lower portion of the deformed Al-4.5Ni pillar (Fig. 5(d)). At the transition zone between the less and severely deformed regions, columns started bending and deflecting from their growth direction (Fig. 5(e)). In the severely deformed pillar top, significant grain rotation and grain fragmentation occurred. ASTAR orientation map (Fig. 5(c)) shows the formation of equiaxed grains on the pillar top induced by deformation. HRTEM images with inserted FFT images (Fig. 5(f-g) show the atomic microstructure of Al_3Ni and Al nanograin.

Similar TEM analyses were performed on the deformed Al-4.5Ni-3Ti pillars. Fig. 6(a-c) show bended columnar grains on pillar top and less deformed columns at the lower portion of the deformed pillar. Moreover, some dislocation networks are indicated by using yellow arrows on the deformed pillar. Equiaxed grains, significant grain coarsening and rotation were not observed on the top of the Al-4.5Ni-3Ti deformed pillar as shown in the ASTAR orientation map (Fig. 6(c)). HRTEM images show less deformed 9R phases with sub-column boundaries in the middle of deformed pillar. Sub-column boundaries (Fig. 6(f)), 9R phases (Fig. 6(g)) and LAGBs (Fig. 6(h)) were frequently observed on the Al-4.5Ni-3Ti deformed pillar top, indicating good stability during deformation.

EDS analyses in Fig. 7 and Fig. S2 reveal solute distributions in the deformed Al-4.5Ni and Al-4.5Ni-3Ti pillars. As shown in Fig. 7(a) and Fig. S2(c), Ni segregation took place on the deformed pillar top of Al-4.5Ni alloy and confirmed in the line scans composition profile (Fig.7(b)). In comparison, solute segregation was absent in the deformed Al-4.5Ni-3Ti pillar as shown in the EDS map (Fig. 7(d), Fig. S2(e-f)) and line scans (Fig. 7(e-f)).

3.4 Thermal stability study

Fig. 8(a) compares the hardnesses of Al-4.5Ni and Al-4.5Ni-3Ti annealed at different temperatures. The hardness of annealed Al-4.5Ni plummeted at 150 °C, suggesting the dramatic microstructure changes in the annealed Al-4.5Ni. Interestingly, the softening temperature was postponed to 300 °C in the Al-4.5Ni-3Ti. After being annealed at 400 °C, the hardness of Al-4.5Ni-3Ti and Al-4.5Ni was ~ 1.9 ± 0.14 GPa and 1.45 ± 0.06 GPa respectively.

Systematic XRD analyses (Fig. 8(b-c)) performed on the annealed samples demonstrate the microstructure evolutions of NT Al-Ni and Al-Ni-Ti alloys. As shown in Fig. 8(b), diffraction peaks from Al_3Ni (orthorhombic) (220), (210) and (221) were observed when the

annealing temperature (T_a) ≥ 150 ℃. In comparison, Al_3Ni peak emerged in the Al-4.5Ni-3Ti when T_a ≥ 300 ℃. Moreover, the peak intensity ratio of Al_3Ni over the Al (111) in the Al-4.5Ni-3Ti alloy is much lower than in Al-Ni alloys, suggesting lower fraction of intermetallics formed in the ternary alloys.

TEM analyses on the annealed Al-4.5Ni (Fig. 9) and Al-4.5Ni-3Ti (Fig. 10) show distinct microstructures. Recrystallization led to nanograins (Fig. 9(a), (d)) with an average grain size of 105 nm (Fig. S3(a)) in the Al-4.5Ni annealed at 150 °C. The Al_3Ni (Fig. 9(b)) and a small number of residual 9R phases (Fig. 9(c)) were observed among recrystallized grains in Al. EDS map shows that Ni solute atoms segregate (Fig. 9(e) in the annealed Al-4.5Ni. In contrast, Al-4.5Ni-3Ti annealed at 250 °C (0.56 T_m^{Al}) still had NT columns (Fig. 10(a-b)) with an average grain size of ~ 36 nm (Fig. S3(b)). High-density 9R phases persist in nanocolumns without the formation of intermetallics (Fig. 10(c)). Moreover, EDS maps (Fig. 10(d-f)) show the uniform distribution of Al, Ni and Ti in the 250℃-annealed Al-4.5Ni-3Ti alloy.

3.5. Density functional theory (DFT) calculations

Stacking fault energy. DFT calculations were performed to calculate the SFE of Al with and without Ti solute atoms on fault plane. Slab models containing 10 layers of FCC {111} planes with 16 atoms on each layer were used to perform this calculation. A 4×4×1 M-P K points grid was employed to integrated first Brillouin zone. By shifting upper 5 layers of {111} planes along <112> direction, 5 models between single crystal configuration and stacking fault configuration were generated. The generalized stacking fault energy was calculated using these models. As shown in Fig. 11(a), the addition of ~ 2 at. % Ti can increase the unstable stacking fault energy (USFE) of Al from 167.7 to 172.2 mJ/m^2. Meanwhile, the stable SFE decreases from 125.7 to 121 mJ/m^2.

Energy of surface heptamer and trimer.

The energy states of surface trimer and heptamer cluster atoms were also investigated. During deposition, adatoms form clusters on the film surface, and the migration and expansion of clusters form the new film surface. The cluster can be located at the perfect sites or stacking fault sites. The stability of stacking faults is related to the energy change of moving surface cluster between these two sites. To compute these energy variations, the model consisted of two layers of {111} planes and surface cluster on the plane. For trimer and heptamer models, each layer of {111} plane contains 16 and 36 atoms respectively with 6×6×3 and 3×3×3 M-P K points grids. The bottom layer of substrate is fixed during relaxion. Calculated excess energies of surface trimer and heptamer are presented in Fig.11 (b-c). The addition of Ti solute modifies the energy profiles of surface trimer and heptamer. Without Ti solute, the migration energy barriers for surface trimer and heptamer is 0.1006 and 0.0977 eV/atom, respectively. And the energy of surface trimer and heptamer at stacking fault sites is -0.0058 and 0.0329 eV/atom, respectively.

Ti solutes increase the migration energy barriers to 0.1367 and 0.1246 eV/atom for trimer and heptamer, respectively. Moreover, the energy of two types of clusters at stable stacking fault positions (coordinate 6) decreases slightly.

Energy of solute pairs near the ITB.

The energy of solute pairs near the ITB was also calculated. As shown in Fig. 11(d), axis of simulation boxes is along $[11\bar{2}]$, $[111]$ and $[1\bar{1}0]$ direction of Al respectively. The reciprocal space was sampled by a 1×4×4 M-P grid. We investigated 25 different configurations with Ni-Ni, Ti-Ti and Ni-Ti pairs at different positions near the ITB. The energy difference (ΔE) between Ni-Ti and pure metal pairs was calculated as:

$$\Delta E = E_{Ni-Ti} - 1/2(E_{Ni-Ni} - E_{Ti-Ti}) \quad (1)$$

Fig. 11 (d-f) show three representative low-energy configurations with corresponding energy difference, and ΔE is -1.150, -1.137 and -1.064 eV/atom, respectively.

4. Discussion

4.1. Strengthening mechanisms

As shown in Fig.1 (d-e), Al-Ni and Al-Ni-Ti alloys have high hardnesses. More specifically, the peak hardness of ternary Al-Ni-Ti alloy reaches 6.8 GPa, the highest hardness reported so far in Al alloys. The high strength of NT Al alloys can be attributed to the solid solution strengthening, nanoscale grain size, and high-density ITBs.

The solid solution strengthening effect of Ti and Ni in Al can be roughly estimated by using Fleischer formula [45]. And our previous studies [24,28] have proved that strengthening due to solid solution strengthening effect of Ni and Ti solutes is limited. Therefore, other factors may play a more dominant role in strengthening Al alloys.

Grain size refinement can bring a significant hardening effect based on the Hall-Petch relation. As shown in Fig. 1(e), the smallest grain size of Al-Ni and Al-Ni-Ti alloys is ~7-8 nm. And the grain size of Al-Ni alloys can be further refined with the addition of Ti solute. As shown in Fig. 2-3, the grain size of Al-4.5Ni decreases from 39 to 30 nm due to the addition of 3 *at.* % Ti. Moreover, abundant sub-column boundaries in Al-4.5Ni-3Ti alloy (Fig. 3(e)) might introduce some hardening effect via introducing slip discontinuity. However, Hall-Petch relation normally breaks down and induces softening when the grain size is below the critical value because of the activation of GB-mediated deformation mechanisms [46,47]. Noticeably, softening was not observed in binary and ternary Al alloys as the grain size decreases below 10 nm due to the presence of high-density 9Rs and ITBs in binary and ternary Al alloys [22,48].

Both MD simulations [26] and *in situ* nanoindentation [20] have shown the blocking effect of ITBs or 9R phase to the transmission of dislocations. Dislocation can pile up against ITBs, resulting in work hardening in pure Al. Li *et al* [26] showed the effect of Fe solute on stabilizing 9R phases and retarding detwinning in Al during deformation. Statistics based on TEM analyses show that the twin fraction in in Al-4.5Ni and Al-4.5Ni-3Ti is 25% and 55% respectively. Therefore, higher twin density may bring extra strengthening effect in Al-4.5Ni-3Ti.

DFT calculations (Fig.11(a)) show that the addition of 2 at.% Ti can slightly reduce the SFE of Al from 125.7 to 121 mJ/m^2, and more importantly, the energy barriers (Fig. 11(b-c)) associated with migration of surface trimers and heptamers increases sharply by 30%, significantly prohibiting the defaulting process for the stacking faults or twin boundaries formed during deposition. As a consequence, the ternary Al alloys have higher twin density than the binary Al-Ni alloy. The influence of Ti solutes on microstructure and mechanical stability of Al-Ni alloys will be discussed in the succeeding sections.

4.2. Deformability of NT Al-Ni-Ti alloy

Significant deformability

Shear bands have been frequently reported in ultra-fine grained (UFG) [49] and NC metallic materials [50] at moderate strain level (ε > 10 %) during pillar compression. In comparison, our studies show that both Al-4.5Ni and Al-4.5Ni-3Ti can deform to over 16 % engineering strain without shear band or catastrophic failure. The good deformability of NT Al alloys may arise from their NT columnar microstructures. TEM analyses show that both Al-4.5Ni and Al-4.5Ni-3Ti have high-density vertical ITBs. ITBs can readily migrate through the glide of Shockley partials at high strain level to carry plasticity. The migration of ITBs may induce grain rotation and grain coarsening as shown in Fig. 5(b) and Fig. 6(c). In addition, the distorted ITBs can serve as the nucleation sites for mobile dislocations to further accommodate plastic deformation [20,51].

When ε >15%, significant localized deformation took place on the Al-4.5Ni pillar top, indicating the deformation instability. Hart's criterion [52] is normally used to describe deformation instability:

$$\frac{1\partial\sigma}{\sigma\partial\varepsilon} + m \geq 1 \quad (2),$$

where σ is the flow stress, ε is the strain, $\frac{\partial\sigma}{\partial\varepsilon}$ is the work hardening rate, and m is strain rate sensitivity. A high work hardening rate can postpone deformation instability. Highly localized deformation in the Al-4.5Ni is due to the work softening triggered by detwinning, phase segregation, and recrystallization on the pillar top. In comparison, localized deformation is insignificant in the Al-4.5Ni-3Ti, demonstrating its better deformability because of a greater work hardening rate (Fig. 4i).

Work hardening capability

Compared with Al-4.5Ni, Al-4.5Ni-3Ti has higher flow stress and greater work hardening capability (Fig. 4(i)). The enhanced work hardening capability can be ascribed to higher twin density and twin stability in the Al-4.5Ni-3Ti alloy.

Due to the insufficient storage capability for dislocations, UFG and NC metallic materials normally have very limited work hardening capability. It has been shown that dislocation can nucleate from GBs in NC materials [30]. However, as confirmed by XRD [53] and *in situ* TEM straining study [54], dislocations nucleating from GBs can readily glide across the grain interior and be absorbed by adjacent GBs, resulting in little increase in dislocation density.

It has been shown that nanotwins enable high work hardening rate [55] and work hardening exponent [56] in NT Cu due to the nucleation and accumulation of dislocations along CTBs. Lu *et al* [56] and Wang *et al* [57] have confirmed increasing dislocation density in deformed NT Cu caused by nucleation of partial dislocations from defective CTBs. Furthermore, interactions of ITBs or CTBs with dislocations and stacking faults can trigger nucleation of partial dislocations, as confirmed by MD simulations [19,20] and *in situ* nanoindentation [52].

Therefore, a higher twin density in Al-4.5Ni-3Ti should give rise to a greater work hardening rate than in Al-4.5Ni. These high-density ITBs may contribute to the increasing work hardening capability through the following mechanisms. First, higher ITB density leads to more intensive interactions between dislocations and ITBs, leaving behind more residual dislocations near ITBs. These defective ITBs can provide storage and nucleation sites for more dislocations. Second, the NT ternary Al alloy has a higher density of ITBs that provide a larger number of mobile partial dislocations. Studies [58] have shown that ITBs consist of array of Shockley partial dislocations, b_1, b_2, and b_3, that are mobile under stress.

Apart from the increasing twin density, the microstructure stability also plays major role on the retention of high work hardening rate in the ternary alloys. As shown in Fig. 5(c) and Fig. 7(a), decomposition and recrystallization led to softening and detwinning in the pillar top of NT Al-4.5Ni. In contrast, NT columns retained in the deformed pillar top of Al-4.5Ni-3Ti as shown in Fig. 6 and Fig. 7(d). The synergetic pinning effect of Ti and Ni solutes on ITBs and GBs may retard detwinning and work softening in the Al-4.5Ni-3Ti alloy. Interestingly, softening on the Al-4.5Ni pillar top did not cause drastic stress drop, mainly because of the high work hardening capability in the lower portion of the Al-4.5Ni pillar with NT columnar structure. Therefore, the combination of work hardening and work softening in the Al-4.5Ni pillar led to a constant flow stress when $\varepsilon > 8\%$. In comparison, the flow stress in the ternary NT Al alloy increases continuously to a large strain value (15%) as shown in Fig. 4(k).

4.3. Microstructure stability improved with the addition of Ti

Improved microstructure stability under deformation

The NT Al-Ni-Ti ternary alloys have superior microstructure stability than the NT Al-Ni alloy under deformation. Post-compression analyses demonstrate distinct deformation induced grain evolution in Al-4.5Ni and Al-4.5Ni-3Ti. More specifically, equiaxed grains replaced the columnar grains in the deformed Al-4.5Ni pillar top. In contrast, the Al-4.5Ni-3Ti has bended columnar grains after deformation. The disparity in deformed microstructures may be related to the thermodynamics and kinetics related to the GBs in the two alloys.

Some of the equiaxed grains in the Al-4.5Ni deformed pillar top are Al_3Ni phase originating from stress induced diffusion of Ni solutes in Al. Other equiaxed grains in the deformed Al-4.5Ni pillar may arise from the migration of column boundaries, and subsequent grain rotation and grain fragmentation. Compared with GBs in NC materials, column boundaries

with large aspect ratio may bend and migrate under stress because of their inherent geometric instability. Furthermore, the bended column boundaries are vulnerable to GB shearing and rotation, resulting in column fragmentation [28]. Due to the large excess free energies stored in GBs, the driving force for grain growth and recrystallization increases dramatically in NC materials compared with coarse-grained materials [32]. Stress-induced grain growth at liquid nitrogen temperature [59] and secondary recrystallization at room temperature [60] have been reported in NC materials.

Prior study showed that uniformly distributed solutes can effectively retard the migration of GBs and TBs during deformation [27]. Post-compression EDS analyses (Fig. 7(a-c), Fig. S2(a-c)) reveal significant Ni segregation in the Al-4.5 Ni deformed pillar. TEM analyses (Fig. 5) show the formation of Al_3Ni intermetallic. In contrast, the Al-4.5Ni-3Ti deformed pillar remained NT solid solution alloy, as evidenced in Fig. 7(d-f) and Fig. S2(e-g). Solute segregation may undermine the pinning effect of Ni solute on migration of columnar GBs in Al-4.5Ni. In contrast, there is no solute segregation in Al-Ni-Ti ternary alloys. Therefore, the uniformly distributed Ti and Ni solutes can help preserve NT columnar microstructures in ternary alloys.

Why does Ni solute segregate easily in Al-4.5 Ni alloy during deformation? First, Ni solute has abnormally high diffusivity in Al compared with other *3d* transition elements, such as Fe, Ti, V [36]. The diffusivity of Ni solute in Al lattice is only slightly greater than that of Al self-diffusion [36]. And the diffusion activation energy (Q_L) for Ni in Al lattice (145 kJ/mol) is comparable to the Al self-diffusion process (120 -144 kJ/mol), and much less than that of Ti diffusion in Al (260 kJ/mol) [61]. Besides, quantum mechanical calculations [62] showed that Ni solute is more inclined to segregate to GBs in Al than other *3d* elements. Second, high-density 9R phase, GBs and partial dislocations in NT Al-4.5Ni may promote the diffusion of Ni solutes.

Prior studies [35] have shown that the diffusion activation energy in nanocrystalline materials is ~1/2 Q_L, where Q_L is the activation energy for lattice diffusion.

Third, deformation-induced dislocations and dislocation movement will further promote Ni diffusion and segregation. Dislocations may provide rapid diffusion paths for Ni atoms. Deformation induced diffusion and solid-state reaction have been reported in Al-Ni systems processed by high pressure torsion (HPT) [63] and high-energy ball milling [64]. It was shown that the diffusion coefficient of Ni in Al matrix can be enhanced by 10^{12} times during the HPT process [65]. Faster diffusion process arises mostly from the deformation-induced defects, such as dislocations, vacancies, and GBs.

Fourth, the supersaturated Al-Ni alloys are at a metastable energy state as the equilibrium solute concentration of Ni in Al is negligible [66]. Thus, the segregation of Ni solute in Al-Ni is energetically favorable. Moreover, the large electronegativity difference between Ni and Al may facilitate the segregation of Ni in Al matrix. The electronegativity of Ni and Al and Ti is 2.09, 1.5, and 1.38 respectively [35]. A large difference in electronegativity indicates Ni in Al prefer to segregate and form intermetallic rather than supersaturated solid solutions [67].

The diffusion coefficient of Ni (D_{Ni}) in NT Al can be calculated using the Arrhenius-type equation [65]:

$$D_{Ni} = D_0 \exp\left(\frac{-Q_{Ni}}{RT}\right) \quad (3),$$

where, D_0 is the pre-exponential factor (4.4×10^{-4} m^2/s for Ni in Al [61]), Q_{Ni} is the activation energy for Ni diffusion in NT Al, and T is the temperature. Here, Q_{Ni} in NT Al alloys is assumed to be 1/2 Q_L, ~ 73 kJ/mol, as GB diffusion mechanism dominates over lattice diffusion. The D_{Ni} in NT Al alloys at room temperature is calculated to be ~ 8.7×10^{-17} m^2/s.

The apparent diffusion coefficient (D'_{Ni}) of Ni in NT Al-4.5Ni during pillar compression can be estimated by using the diffusion distance (x), and the diffusion time (t) [68]:

$$D'_{Ni} = \frac{x^2}{t} \quad (4),$$

where diffusion distance (x) is estimated to be the grain size (39 nm) because EDS maps show Ni tend to segregate to neighboring GBs, and diffusion time (t) is ~30 s (during the typical cycle of micropillar compression test). By using Eq. (4), D'_{Ni} is estimated to be ~5.1×10^{-17} m^2/s, comparable to the calculated diffusion coefficient of Ni using Eq. (3). Ni segregation was absent in the deformed NT Al-4.5Ni-3Ti pillars due to the pinning effect of Ti solutes, to be discussed in detail later.

Improved thermal stability

NC materials often have poor thermal stability. Prior studies have reported recrystallization, significant grain growth and mechanical softening at 100 -200 °C in NC and UFG Al alloys fabricated by SPD [69,70] or mechanical alloying [71,72]. Our annealing studies (Fig. 8(a)) show that Ti solutes can significantly postpone the mechanical softening of NT Al-Ni alloys from 100-150 °C to 250 - 300 °C. The softening of annealed NT Al alloys is mainly a consequence of solute segregation, detwinning and recrystallization. XRD analyses (Fig. 8(a-c)) show that the critical temperature for the intermetallic formation can be increased from 150 ℃ in the Al-Ni alloys to 300 ℃ in the Al-Ni-Ti alloys.

As shown in Fig. 9, NT Al-4.5Ni fully recrystallized at 150 °C and the grain size increased to 105 nm. In contrast, the Al-4.5Ni-3Ti remained NT structure (Fig. 10) with high-density 9R phases at 250 °C (0.56 T_m^{Al}), and the average grain size is 36 nm (Fig. S3), only slightly larger than the as-deposited alloy. TEM analyses in Fig. 10 further prove that the recrystallization and segregation temperatures have been increased to 300 °C in the ternary alloy.

Unlike the deformation induced recrystallization and grain growth, microstructure evolutions caused by annealing are mainly controlled by thermal-driven diffusion process. And studies have shown that the apparent activation energy for boundary migration in solid solution alloy during annealing is close to the diffusion activation energy of solutes [73]. Therefore, the thermal stability of Al-Ni binary alloys is limited by the low diffusion activation energy (145 kJ/mol) of Ni solute in Al. Meanwhile, the improved thermal stability of Al-Ni-Ti alloy indicates that activation energies for the diffusion processes and the migration of GBs have been increased because of the Ti solutes. The next puzzle is why Ti can improve the thermal stability of binary Al alloys?

4.4. Synergetic alloying effect of Ni and Ti solutes

The current study shows that the addition of Ti solute can enhance the microstructure stability of Al-Ni alloys under deformation and heat treatment. The synergetic alloying effects may arise from several aspects. First, Ti is more stable and less reluctant to segregate than Ni in Al. Second, Ti solute might retard the diffusion and segregation of Ni solute. Third, low-energy Ni-Ti pairs can effectively stabilize ITBs and GBs.

Ti: A sluggish solute in Al

Ti solutes prefer to distribute uniformly and form solid solution Al alloys, partially related to their small electronegativity difference [37,67,74] (Ti 1.38, Al 1.5) and similar atomic radii (Ti 0.147 nm, Al 0.143 nm). Furthermore, the diffusion of these uniformly distributed Ti solutes in Al is more sluggish than Ni solutes. The diffusivity of Ti in Al is several orders of magnitude smaller than that of Ni in Al. And the diffusion coefficient of Ti and Ni in Al at 400 °C is ~ 10^{-34} m^2/s and ~10^{-24} m^2/s respectively. The smaller diffusivity of Ti is due to its large diffusion activation energy barrier that is proportional to the bonding strength between solute atoms and nearest Al atoms. First-principle calculations [37,38,75] have shown that the boding strength is

closely related to the electron density states of *d* orbitals, the *d*-orbital energy level (*Md*), and the bond order of transition metals. It has been shown that Ti has a much higher *d*-orbital electron density and energy level than Ni [75,76]. Moreover, Moringa *et al* [37] proved that Ti has the largest bond order (~1.2) with Al among 3d transition metals, much higher than that of Ni (0.25).

The effect of Ti solute on the diffusion of Ni solute

As mentioned earlier, Ti solutes are more stable than Ni solutes in Al. Furthermore, it is likely that these stable Ti solutes may retard the diffusion of Ni in Al matrix. In ternary Al-Ni-Ti alloys, Ti atoms may bond with either Al or Ni atoms. Cluster calculation results [68] proved that Ni-Ti bond has higher *d*-orbital energy level (2.27 eV) and bond order (1.098) than Ni-Al bond (1.90 eV and 0.533 respectively). Therefore, Ni-Ti pairs should have higher bonding strength than Ni-Al pairs. Consequently, stronger Ni-Ti interatomic bond might increase the diffusion activation energy barriers and lower diffusivity of Ni atoms in Al-Ni-Ti ternary alloys. Similar phenomenon has been reported in Al-Ni-Ce [77] system, where the mobility and diffusivity of Ni atoms were decreased due to the addition of Ce solutes.

Synergetic pinning effect of Ni-Ti pairs on ITBs

Though the diffusion of Ni and Ti solutes in the Al matrix has been investigated before [61,62], how would solutes interact with GBs and ITBs in Al remains unknown. Therefore, we have performed in-depth DFT analyses on energy states of solute pairs near the ITBs. Our DFT calculation results (Fig. 11(d-e)) show that the Ni-Ti solute pairs have lower formation energies than the Ti-Ti and Ni-Ni pairs near the ITBs. Thus, the Ni-Ti solute pairs near ITBs are more stable and less likely to segregate than Ni solute pairs alone, leading to a sluggish solute diffusion process and a robust synergetic pinning effect on migration of GBs and ITBs. During the deformation and annealing, these synergetic Ni-Ti pairs may significantly decrease the

mobility of adatoms and increase the migration energy barriers of ITBs and GBs, leading to the improved microstructure stability.

5. Conclusions

This study suggests that the mechanical properties and thermal stability of Al alloys can be upgraded by proper alloying. We have fabricated the high-strength Al-Ni-Ti alloys with a peak hardness of 6.8 GPa and significant deformability. The ternary Al-Ni-Ti alloys have superior microstructure stability than their binary Al-Ni alloys counterparts under deformation and heat treatment. DFT calculations prove that the improved microstructure stability arises from the synergetic pinning effects of Ni-Ti solute pairs along grain boundaries and twin boundaries. This study may shed light on the design of high-strength, lightweight, and thermally stable alloys through synergetic alloying with solute pairs.

Conflicts of interest

There are no conflicts of interest to declare.

Acknowledgement

This work is supported by the Department of Energy - Basic Energy Science (DOE Award number: DE-SC0016337). Accesses to the Microscopy Facilities at Purdue University and Center for Integrated Nanotechnologies (managed by Los Alamos National Laboratory) are also acknowledged.

References

1 C. Y. Seemikeri, S. B. Mahagaonkar and P. K. Brahmankar, *Int. J. Surf. Sci. Eng.*, 2010, **4**, 465–491.

2 T. Engdahl, V. Hansen, P. J. Warren and K. Stiller, *Mater. Sci. Eng. A*, 2002, **327**, 59–64.

3 W. Sun, Y. Zhu, R. Marceau, L. Wang, Q. Zhang, X. Gao and C. Hutchinson, *Science (80-.).*, 2019, **363**, 972–975.

4 Y. Sun, M. Aindow, R. J. Hebert, T. G. Langdon and E. J. Lavernia, *J. Mater. Sci.*, 2017, **52**, 12170–12184.

5 V. V. Stolyarov, R. Lapovok, I. G. Brodova and P. F. Thomson, *Mater. Sci. Eng. A*, 2003, **357**, 159–167.

6 P. V. Liddicoat, X. Z. Liao, Y. Zhao, Y. Zhu, M. Y. Murashkin, E. J. Lavernia, R. Z. Valiev and S. P. Ringer, *Nat. Commun.*, 2010, **1**, 63.

7 T. T. Sasaki, T. Ohkubo and K. Hono, *Acta Mater.*, 2009, **57**, 3529–3538.

8 S. C. Pun, W. Wang, A. Khalajhedayati, J. D. Schuler, J. R. Trelewicz and T. J. Rupert, *Mater. Sci. Eng. A*, 2017, **696**, 400–406.

9 M. Zawrah and L. Shaw, *Mater. Sci. Eng. A*, 2003, **355**, 37–49.

10 L. Lu, Y. Shen, X. Chen, L. Qian and K. Lu, *Science (80-.).*, 2004, **304**, 422–426.

11 X. Zhang, A. Misra, H. Wang, T. D. Shen, M. Nastasi, T. E. Mitchell, J. P. Hirth, R. G. Hoagland and J. D. Embury, *Acta Mater.*, 2004, **52**, 995–1002.

12 Q. Li, S. Xue, P. Price, X. Sun, J. Ding, Z. Shang, Z. Fan, H. Wang, Y. Zhang, Y. Chen, H. Wang, K. Hattar and X. Zhang, *Nanoscale*, , DOI:10.1039/C9NR07472D.

13 D. Bufford, H. Wang and X. Zhang, *Acta Mater.*, 2011, **59**, 93–101.

14 O. Anderoglu, A. Misra, H. Wang and X. Zhang, *J. Appl. Phys.*, 2008, **103**, 94322.

15 Y. F. Zhang, R. Su, T. J. Niu, N. A. Richter, S. Xue, Q. Li, J. Ding, B. Yang, H. Wang and X. Zhang, *Scr. Mater.*, 2020, **186**, 219–224.

16 Q. Li, J. Cho, S. Xue, X. Sun, Y. Zhang, Z. Shang, H. Wang and X. Zhang, *Acta Mater.*, 2019, **165**, 142–152.

17 X. Zhang, K. Hattar, Y. Chen, L. Shao, J. Li, C. Sun, K. Yu, N. Li, M. L. Taheri, H. Wang, J. Wang and M. Nastasi, *Prog. Mater. Sci.*, 2018, 96, 217–321.

18 T. Niu, J. Li, Y. Zhang, J. Cho, J. Ding, R. Su, S. Xue, C. Fan, Z. Shang and D. Chen, *J. Nucl. Mater.*, 2020, 152392.

19 Z. H. Jin, P. Gumbsch, K. Albe, E. Ma, K. Lu, H. Gleiter and H. Hahn, *Acta Mater.*, 2008, **56**, 1126–1135.

20 D. Bufford, Y. Liu, J. Wang, H. Wang and X. Zhang, *Nat. Commun.*, 2014, **5**, 4864.

21 H. Rösner, J. Markmann and J. Weissmüller, *Philos. Mag. Lett.*, 2004, **84**, 321–334.

22 Y. F. Zhang, S. Xue, Q. Li, J. Li, J. Ding, T. J. Niu, R. Su, H. Wang and X. Zhang, *Acta Mater.*, 2019, **175**, 466–476.

23 S. Xue, Z. Fan, Y. Chen, J. Li, H. Wang and X. Zhang, *Acta Mater.*, 2015, **101**, 62–70.

24 Y. F. Zhang, S. Xue, Q. Li, C. Fan, R. Su, J. Ding, H. Wang, H. Wang and X. Zhang, *Scr. Mater.*, 2018, **148**, 5–9.

25 S. Xue, Q. Li, Z. Fan, H. Wang, Y. Zhang, J. Ding, H. Wang and X. Zhang, *J. Mater. Res.*, 2018, **33**, 3739–3749.

26 Q. Li, S. Xue, J. Wang, S. Shao, A. H. Kwong, A. Giwa, Z. Fan, Y. Liu, Z. Qi, J. Ding, H. Wang, J. R. Greer, H. Wang and X. Zhang, *Adv. Mater.*, , DOI:10.1002/adma.201704629.

27 S. Xue, Q. Li, D. Y. Xie, Y. F. Zhang, H. Wang, H. Wang, J. Wang and X. Zhang, *Mater. Res. Lett.*, 2019, **7**, 33–39.

28 Y. F. Zhang, Q. Li, S. C. Xue, J. Ding, D. Y. Xie, J. Li, T. Niu, H. Wang, H. Wang, J. Wang and X. Zhang, *Nanoscale*, 2018, **10**, 22025–22034.

29 L. S. Toropova, D. G. Eskin, M. L. Kharakterova and T. V. Dobatkina, *Adv. Alum. Alloy. Contain. Scandium Struct. Prop.*, 2017, 1–175.

30 M. A. Meyers, A. Mishra and D. J. Benson, *Prog. Mater. Sci.*, 2006, 51, 427–556.

31 A. R. Kalidindi and C. A. Schuh, *Acta Mater.*, 2017, **132**, 128–137.

32 M. Ames, J. Markmann, R. Karos, A. Michels, A. Tschöpe and R. Birringer, *Acta Mater.*, 2008, **56**, 4255–4266.

33 A. Devaraj, W. Wang, R. Vemuri, L. Kovarik, X. Jiang, M. Bowden, J. R. Trelewicz, S. Mathaudhu and A. Rohatgi, *Acta Mater.*, 2019, **165**, 698–708.

34 P. C. Millett, R. P. Selvam and A. Saxena, *Acta Mater.*, 2007, **55**, 2329–2336.

35 N. Moelans, B. Blanpain and P. Wollants, *Acta Mater.*, 2007, **55**, 2173–2182.

36 M. Mantina, S. L. Shang, Y. Wang, L. Q. Chen and Z. K. Liu, *Phys. Rev. B*, 2009, **80**, 184111.

37 M. Moringa, S. Nasu, H. Adachi, J. Saito and N. Yukawa, *J. Phys. Condens. Matter*, 1991, **3**, 6817–6828.

38 A. J. Nathan and A. Scobell, *How China sees America*, Springer Science & Business Media, 2012, vol. 91.

39 P. E. Blöchl, *Phys. Rev. B*, 1994, **50**, 17953.

40 J. D. Pack and H. J. Monkhorst, *Phys. Rev. B*, 1977, **16**, 1748–1749.

41 D. C. Langreth and M. J. Mehl, *Phys. Rev. B*, 1983, **28**, 1809–1834.

42 J. P. Perdew, K. Burke and M. Ernzerhof, *Phys. Rev. Lett.*, 1996, **77**, 3865–3868.

43 M. H. Shaeri, M. T. Salehi, S. H. Seyyedein, M. R. Abutalebi and J. K. Park, *Mater. Des.*, 2014, **57**, 250–257.

44 M. Y. Murashkin, A. R. Kil'mametov and R. Z. Valiev, *Phys. Met. Metallogr.*, 2008, **106**, 90.

45 R. L. Fleischer, *Acta Metall.*, 1966, **14**, 1867–1868.

46 J. R. Trelewicz and C. A. Schuh, *Acta Mater.*, 2007, **55**, 5948–5958.

47 C. E. Carlton and P. J. Ferreira, *Acta Mater.*, 2007, **55**, 3749–3756.

48 Y. F. Zhang, Q. Li, M. Gong, S. Xue, J. Ding, J. Li, J. Cho, T. Niu, R. Su and N. A. Richter, *Appl. Surf. Sci.*, 2020, 146776.

49 M. Mieszala, G. Guillonneau, M. Hasegawa, R. Raghavan, J. M. Wheeler, S. Mischler, J. Michler and L. Philippe, *Nanoscale*, 2016, **8**, 15999–16004.

50 D. Jang and J. R. Greer, *Scr. Mater.*, 2011, **64**, 77–80.

51 N. Li, J. Wang, J. Y. Huang, A. Misra and X. Zhang, *Scr. Mater.*, 2011, **64**, 149–152.

52 E. W. Hart, *Acta Metall.*, 1967, **15**, 351–355.

53 Z. Budrovic, H. Van Swygenhoven, P. M. Derlet, S. Van Petegem and B. Schmitt, *Science (80-.).*, 2004, **304**, 273–276.

54 K. S. Kumar, S. Suresh, M. F. Chisholm, J. A. Horton and P. Wang, *Acta Mater.*, 2003, **51**, 387–405.

55 X. H. Chen and L. Lu, *Scr. Mater.*, 2007, **57**, 133–136.

56 L. Lu, X. Chen, X. Huang and K. Lu, *Science (80-.).*, 2009, **323**, 607–610.

57 Y. Morris Wang, F. Sansoz, T. Lagrange, R. T. Ott, J. Marian, T. W. Barbee and A. V. Hamza, *Nat. Mater.*, 2013, **12**, 697–702.

58 J. Wang, O. Anderoglu, J. P. Hirth, A. Misra and X. Zhang, *Appl. Phys. Lett.*, 2009, **95**, 93–96.

59 K. Zhang, J. R. Weertman and J. A. Eastman, *Appl. Phys. Lett.*, 2005, **87**, 61921.

60 B. Günther, A. Kumpmann and H. D. Kunze, *Scr. Metall. Mater.*, 1992, **27**, 833–838.

61 D. Simonovic and M. H. F. Sluiter, *Phys. Rev. B - Condens. Matter Mater. Phys.*, 2009, **79**, 54304.

62 R. Mahjoub, K. J. Laws, N. Stanford and M. Ferry, *Acta Mater.*, 2018, **158**, 257–268.

63 K. Edalati, S. Toh, M. Watanabe and Z. Horita, *Scr. Mater.*, 2012, **66**, 386–389.

64 K. S. Mohammed, H. T. Naeem and S. N. Iskak, *Phys. Met. Metallogr.*, 2016, **117**, 795–804.

65 K. Oh-Ishi, K. Edalati, H. S. Kim, K. Hono and Z. Horita, *Acta Mater.*, 2013, **61**, 3482–3489.

66 A. S. Ramos, A. J. Cavaleiro, M. T. Vieira, J. Morgiel and G. Safran, *Thin Solid Films*, 2014, **571**, 268–274.

67 Q. Ding, Y. Zhang, X. Chen, X. Fu, D. Chen, S. Chen, L. Gu, F. Wei, H. Bei, Y. Gao, M. Wen, J. Li, Z. Zhang, T. Zhu, R. O. Ritchie and Q. Yu, *Nature*, 2019, 574, 223–227.

68 H. Mehrer, *Diffusion in solids: fundamentals, methods, materials, diffusion-controlled processes*, Springer Science & Business Media, 2007, vol. 155.

69 M. R. Shankar, S. Chandrasekar, A. H. King and W. D. Compton, *Acta Mater.*, 2005, **53**, 4781–4793.

70 V. Randle, in *Metallurgical Transactions A*, Trans Tech Publ, 1990, vol. 21, pp. 2215–2221.

71 F. Zhou, X. Z. Liao, Y. T. Zhu, S. Dallek and E. J. Lavernia, *Acta Mater.*, 2003, **51**, 2777–2791.

72 I. Roy, M. Chauhan, E. J. Lavernia and F. A. Mohamed, *Metall. Mater. Trans. A Phys. Metall. Mater. Sci.*, 2006, **37**, 721–730.

73 A. Rollett, F. Humphreys, G. S. Rohrer and M. Hatherly, *Recrystallization and Related Annealing Phenomena: Second Edition*, Elsevier, 2004.

74 R. E. Watson and L. H. Bennett, *Phys. Rev. B*, 1978, **18**, 6439–6449.

75 R. Drautz and D. G. Pettifor, *Phys. Rev. B - Condens. Matter Mater. Phys.*, 2006, **74**, 174117.

76 N. Sandberg and R. Holmestad, *Phys. Rev. B*, 2006, **73**, 14108.

77 W. Chen, L. Zhang and Y. Du, *Calphad Comput. Coupling Phase Diagrams Thermochem.*, 2016, **52**, 159–168.

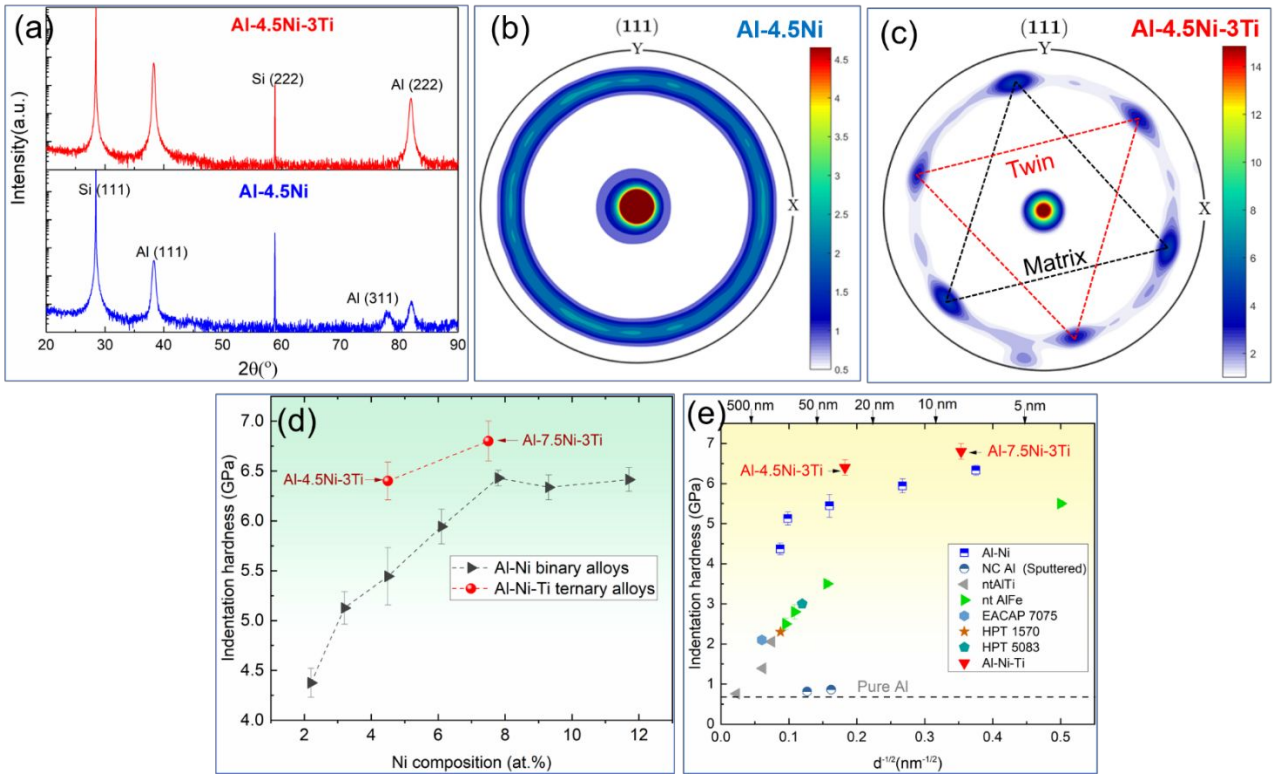

Figure 1. (a) XRD patterns showing Al-4.5Ni-3Ti alloy has enhanced out-of-plane {111} texture compared with Al-4.5Ni alloy. (b-c) XRD pole figure profiles showing the highly {111} textured and nanotwinned Al-4.5Ni-3Ti, and highly-textured Al-4.5Ni alloys.

(d) Hardnesses of binary and ternary Al alloys plotted against the Ni composition.(e) Hardnesses plotted as a function of $d^{-1/2}$ (d is grain size) for nanotwinned Al-Ni-Ti, Al-Ni [23], Al-Ti [19], Al-Fe alloys [21], and bulk nanocrystalline Al alloys [6, 38-39].

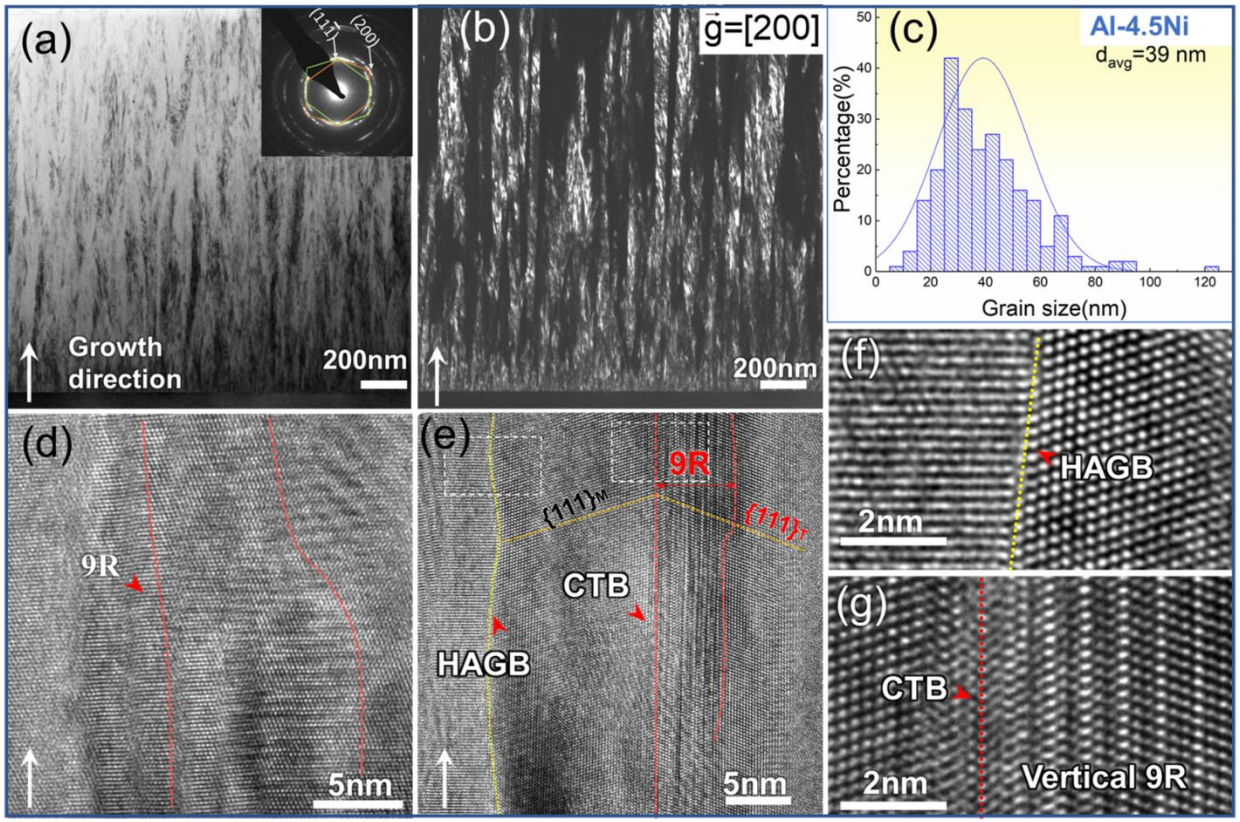

Figure 2. Cross-section TEM (XTEM) studies of as-deposited Al-4.5Ni sample. (a-b) Bright-field (BF) and dark-field (DF) XTEM images showing the formation of nanoscale columnar grains. (c) Statistical distribution indicating an average columnar grain size of 39 nm. (d) High-resolution TEM (HRTEM) image showing a 9R phase (broad ITB). Nearly 25% percent of columns contain 9R phases. (e) HRTEM image presenting a high-angle grain boundary (HAGB) and a vertical CTB and 9R phases along the growth direction (indicated by the white arrow). (f-g) HRTEM images showing the HAGB and 9R phase.

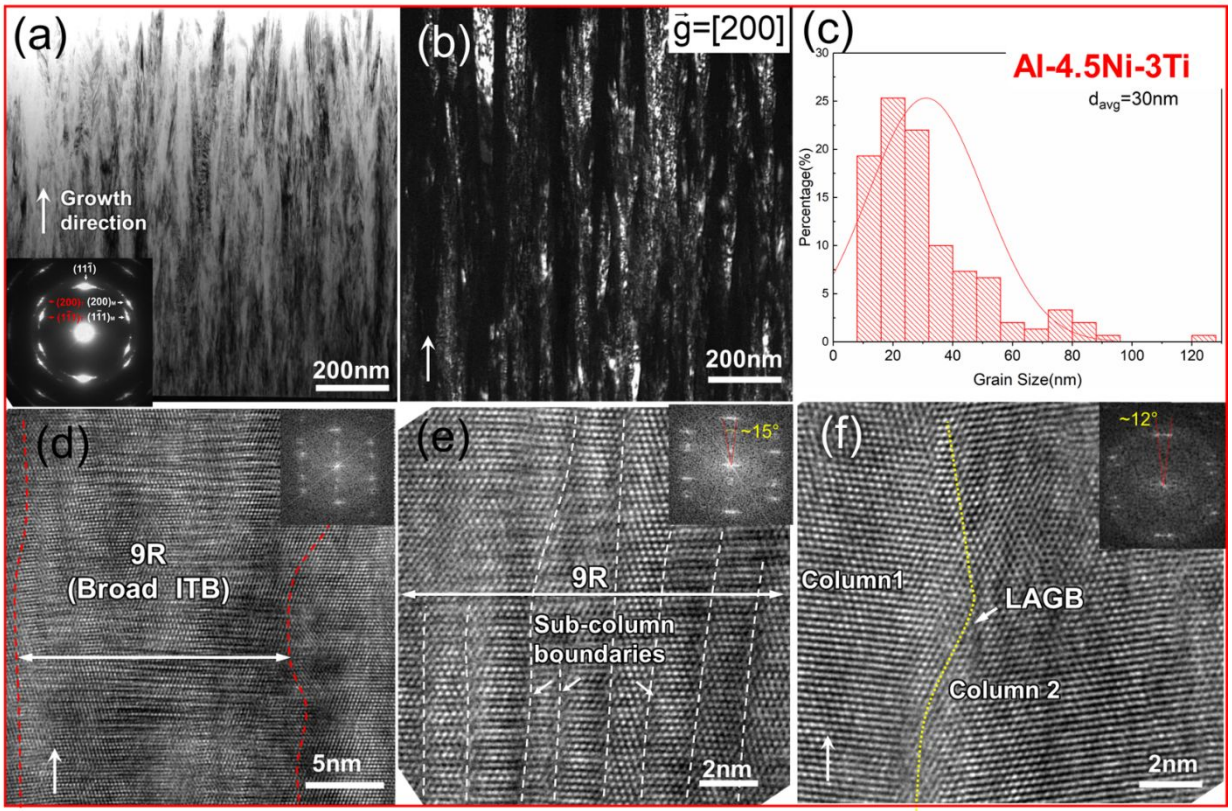

Figure 3. XTEM micrographs of as-deposited Al-4.5Ni-3Ti alloy. (a-b) BF and DF XTEM images revealing nanotwinned columns in Al-4.5Ni-3Ti alloy. (c) Grain size statistics demonstrating an average columnar grain size of 30 nm. (d) HRTEM micrograph showing the broad 9R phase. (e) 9R phases separated by sub-column boundaries (shown by white dash line) with a rotation of 15° among the sub-columns. (f) HRTEM image presenting a low-angle grain boundary (LAGB) between two columns with a misorientation angle of ~12°.

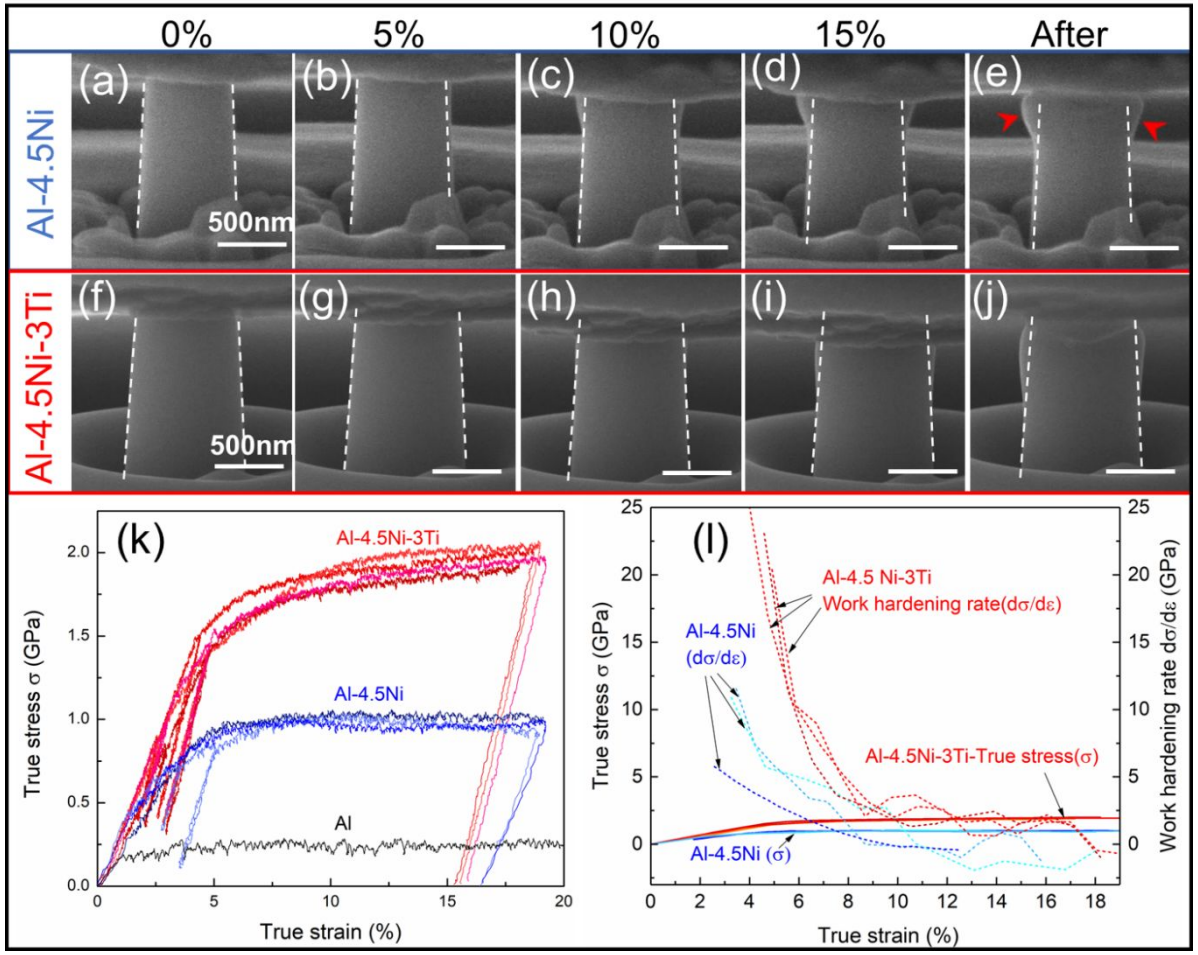

Figure 4. *In situ* micropillar compression studies on Al-4.5Ni and Al-4.5Ni-3Ti alloys. (a-e) SEM video snapshots showing the localized deformation on the pillar top of deformed Al-4.5Ni. (f-j) Morphology evolutions of the Al-4.5Ni-3Ti pillar during pillar compression. (c) True stress-strain curves of Al, Al-4.5Ni, and Al-4.5Ni-3Ti alloys. (d) Work hardening rate ($d\sigma/d\varepsilon$) and true stress (σ) of Al-4.5Ni and Al-4.5Ni-3Ti alloys plotted as a function of the true strain.

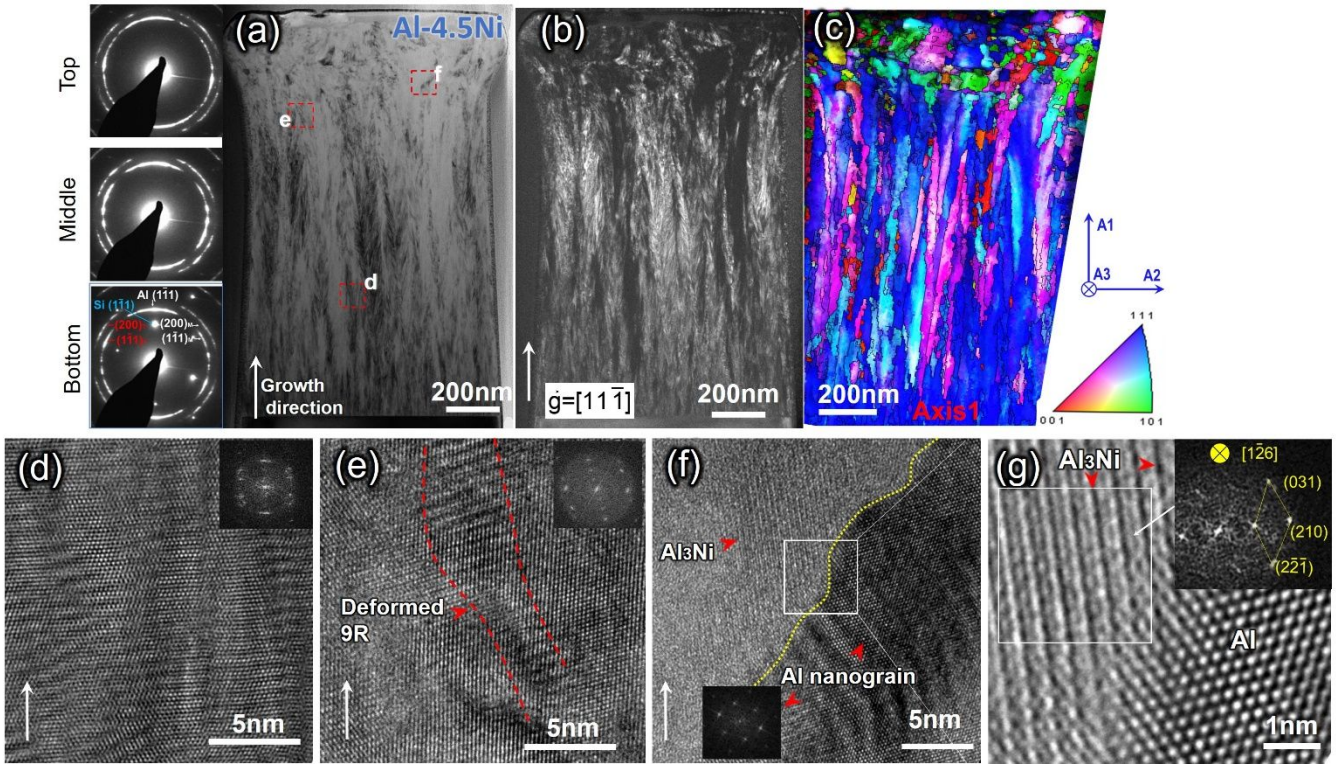

Figure 5. Post-compression TEM analyses of the Al-4.5Ni deformed pillar (to a strain of 17%). (a-b) BF and corresponding DF XTEM images with the inserted selected area diffraction (SAD) pattern showing the dilation and grain rotation and fragmentation near the pillar top. SAD pattern near the pillar base shows the retention of growth twins. (c) ASTAR inverse pole figure (IPF) (in-plane A1 axis) shows the equiaxed grains in the deformed pillar top, and columnar grains in the undeformed pillar base. (d) HRTEM image presenting the slightly distorted 9R phase near the pillar base. (e) The retention of 9R in a transition zone between deformed and less deformed region. (f-g) HRTEM micrographs displaying the recrystallized nanograins and the formation of Al_3Ni intermetallic. White arrows indicate the growth direction.

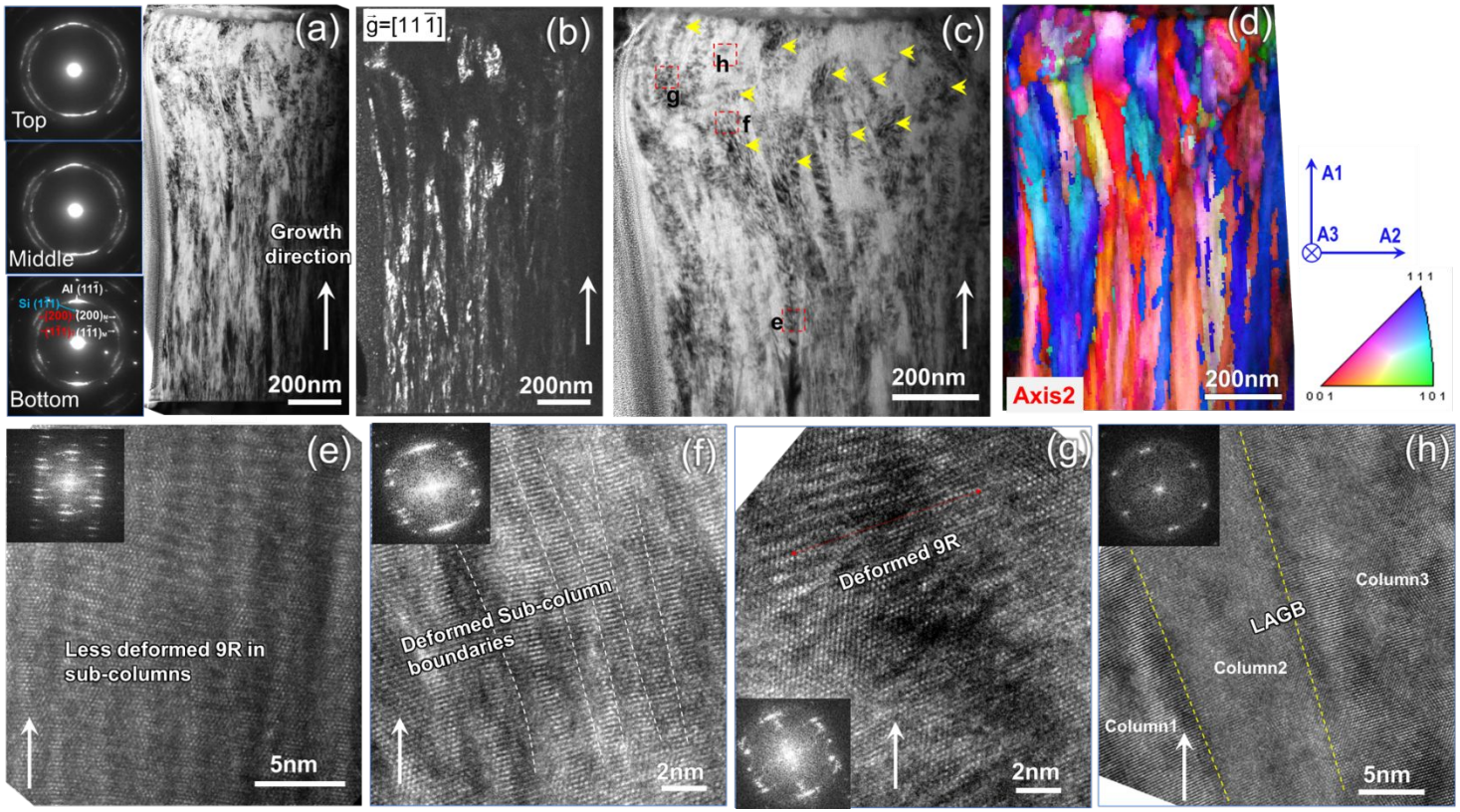

Figure 6. Post-compression TEM analyses of a deformed Al-4.5Ni-3Ti pillar. (a-b) BF and DF XTEM images with SAD patterns showing less dilation and grain rotation near the pillar top. (c) Magnified BF-XTEM micrograph of the top and middle portion of the deformed pillar showing some dislocation networks indicated by yellow arrows. (d) ASTAR IPF map showing crystal orientation of deformed Al-4.5Ni-3Ti pillar from the in-plane axis 2. (e) HRTEM image and inserted fast Fourier transform (FFT) showing less-deformed 9R phase with sub-column boundaries. (f) HRTEM micrograph showing deformed sub-column boundaries at the deformed pillar top. (g) Distorted 9R at the deformed pillar top. (h) HRTEM image showing columnar grains separated by LAGBs at the deformed pillar top.

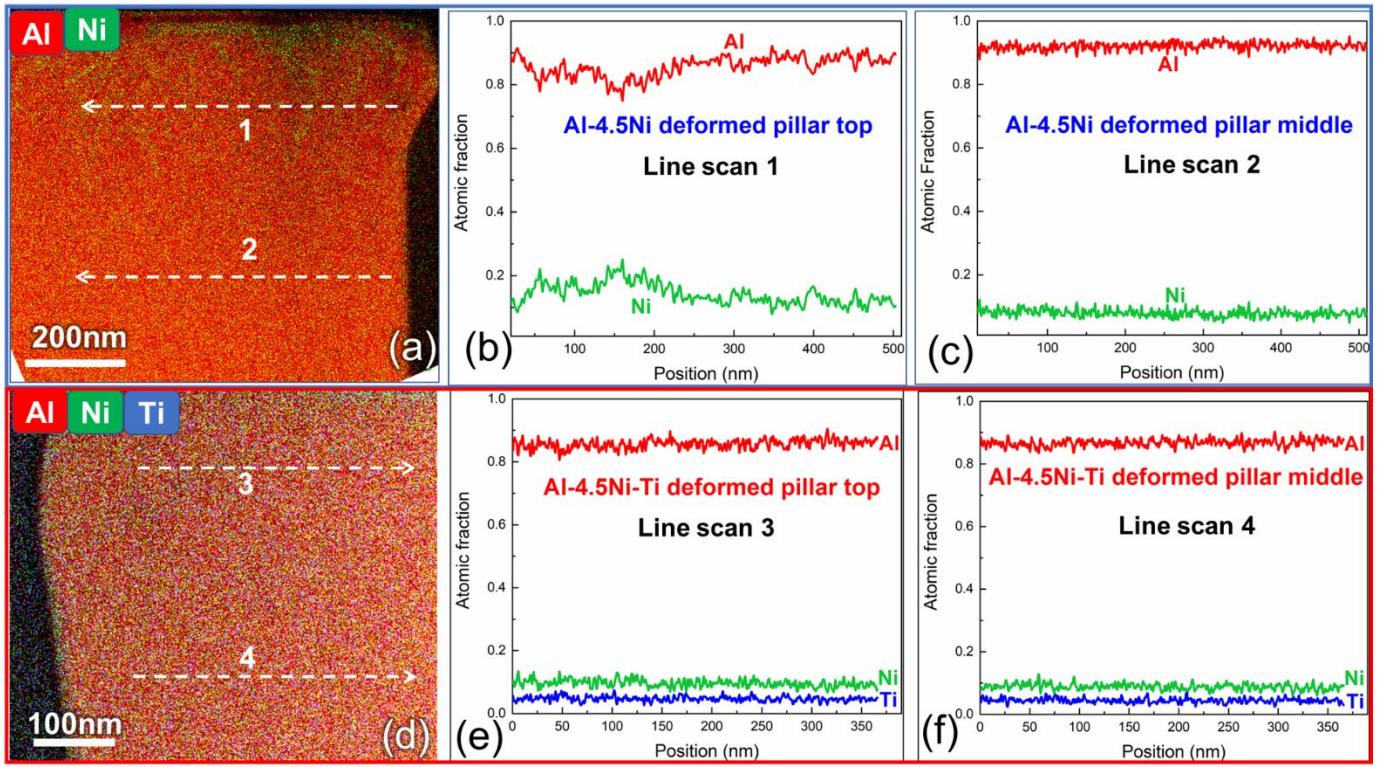

Figure 7. EDS analyses of the deformed Al-4.5Ni and Al-4.5Ni-3Ti pillars. (a-c) EDS map and line scans showing segregation of Ni solutes at the deformed pillar top, and uniform distribution of Ni in the less deformed region. (d-f) EDS map and line scans reveal the more uniform distribution of Ni and Ti solutes both in the top and middle of the deformed Al-4.5Ni-3Ti pillar.

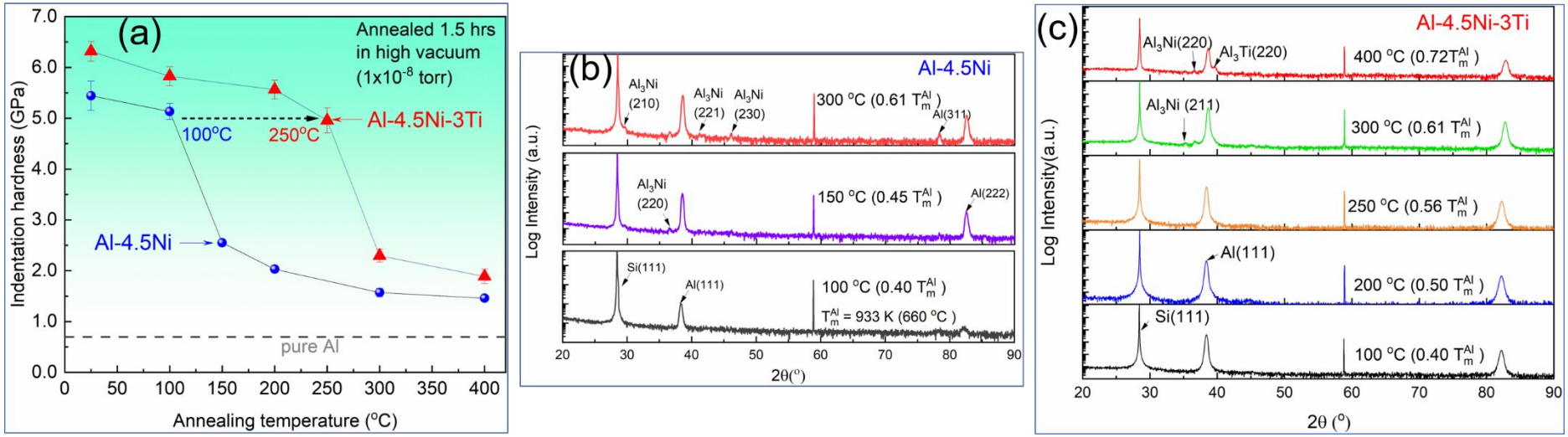

Figure 8. (a) Hardnesses of Al-4.5 Ni and Al-4.5Ni-3Ti alloys annealed at different temperatures. (b-c) XRD scans of Al-4.5Ni alloys and Al-4.5Ni-3Ti alloys annealed at different temperatures under the high vacuum for 1.5 h. Intensities in all XRD plots are plotted in the natural logarithmic scale in all XRD scan profiles.

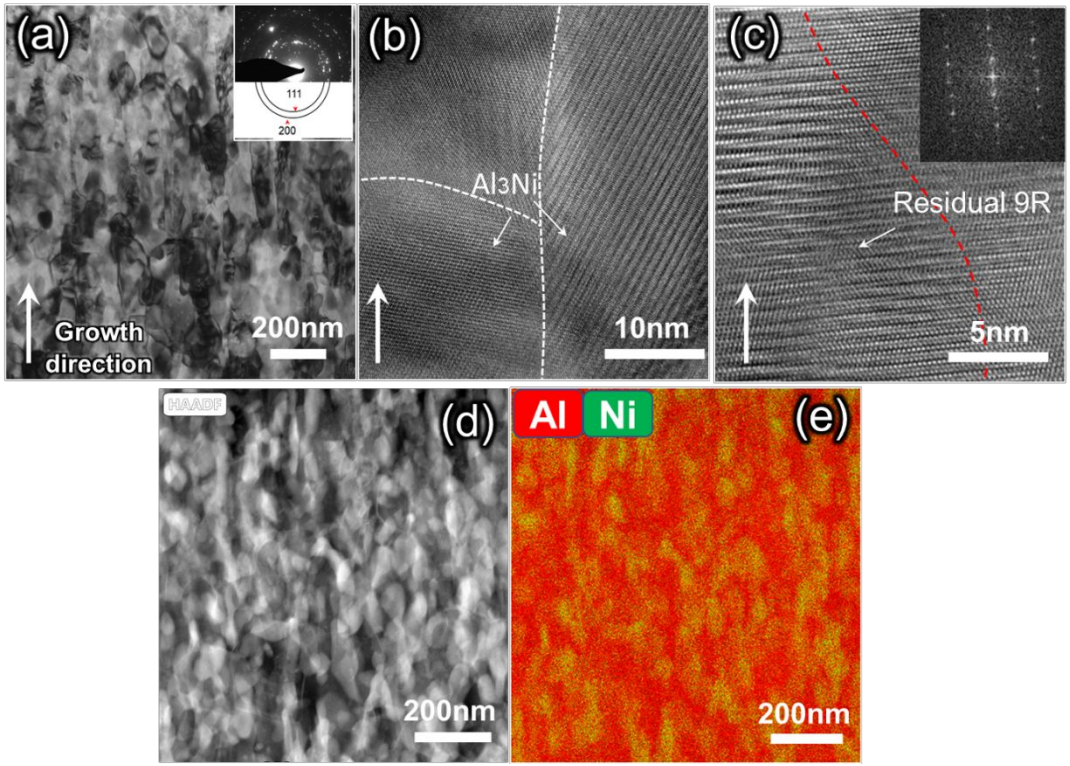

Figure 9. Microstructures of the annealed (150 °C / 1.5 h) Al-4.5Ni alloy. (a) XTEM micrograph showing recrystallized nanograins. (b) HRTEM micrograph showing Al_3Ni intermetallics. (c) HRTEM image revealing a small amout of residual 9R phase. (d) HAADF image of nanograins with an average grain size of 105 nm . (e) EDS map showing Ni solute segregation.

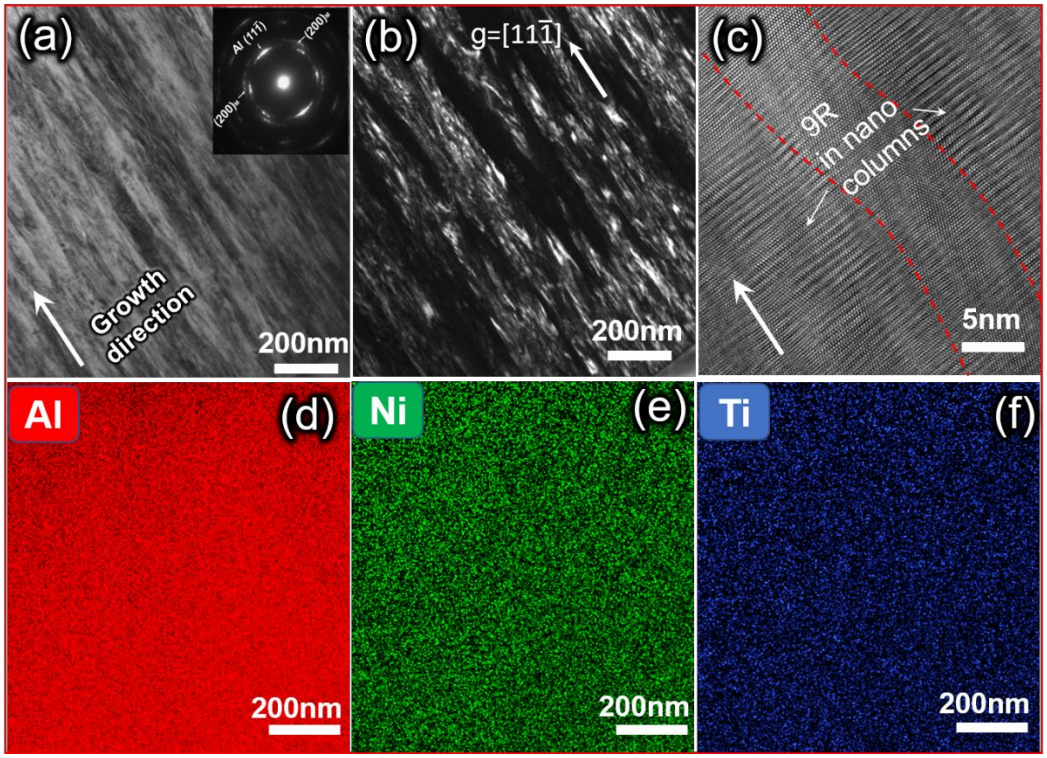

Figure 10. Microstructures of annealed (250 °C / 1.5 h) Al-4.5Ni-3Ti alloy. (a-b) BF and DF XTEM images of nanotwinned columns with an average grain size of 36 nm. (c) HRTEM image showing the retention of high-density 9R phase in nanoscale columnar grains. (d-f) EDS maps proving the uniform distribution of Al, Ni and Ti.

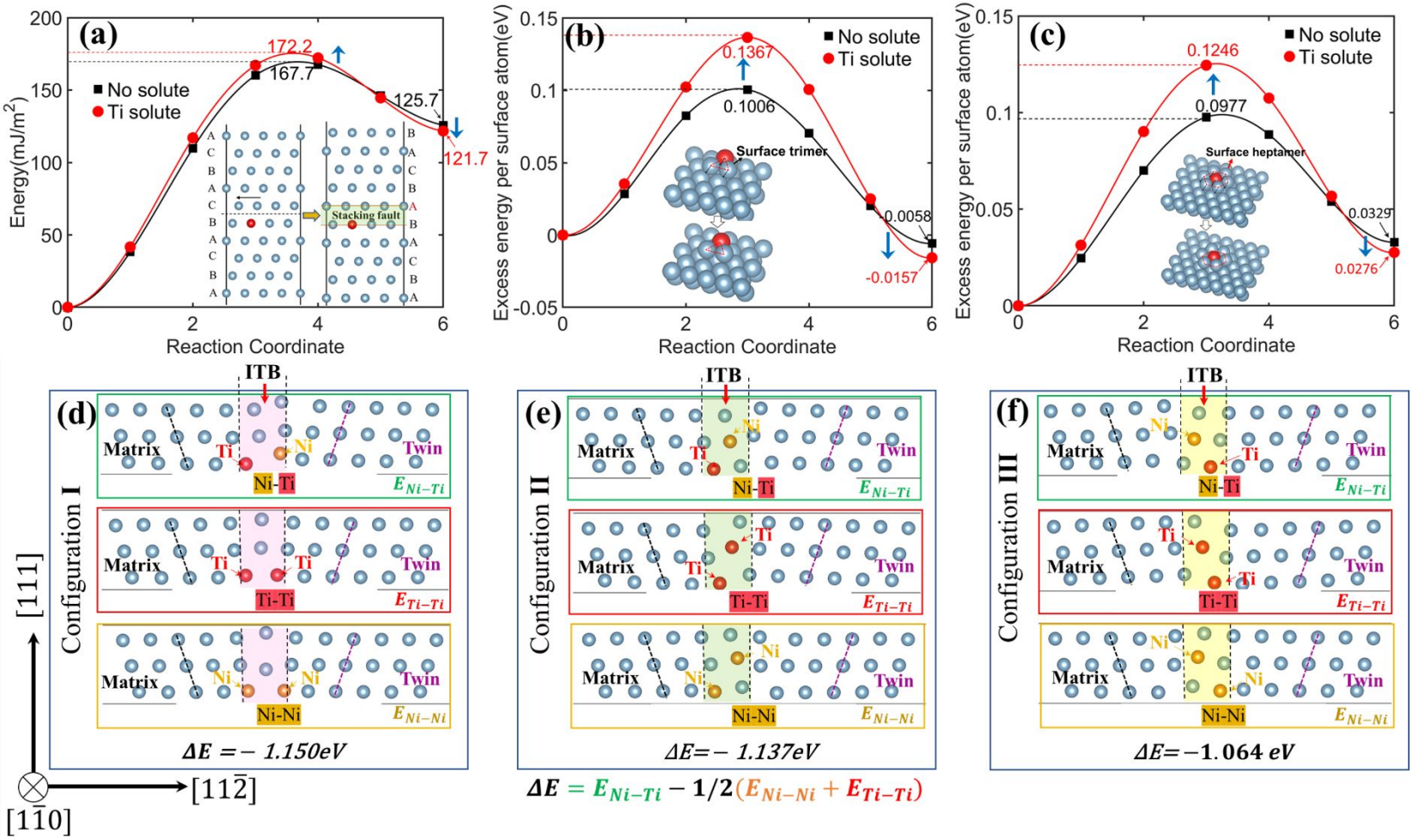

Figure 11. DFT calculation of solute impacts in Al alloy. (a) Slab models and calculated generalized stacking fault energy of Al with and without Ti solute as a function of the reaction coordinates. 0 - 6 corresponds to the FCC structure, and stacking fault structures. (b-c) The excess energy change per surface atom with respect to reaction coordinate for surface trimer and heptamer. (d-f) Three representative atomic configurations showing soltue pairs near the ITBs with corresponding calculated energy difference.

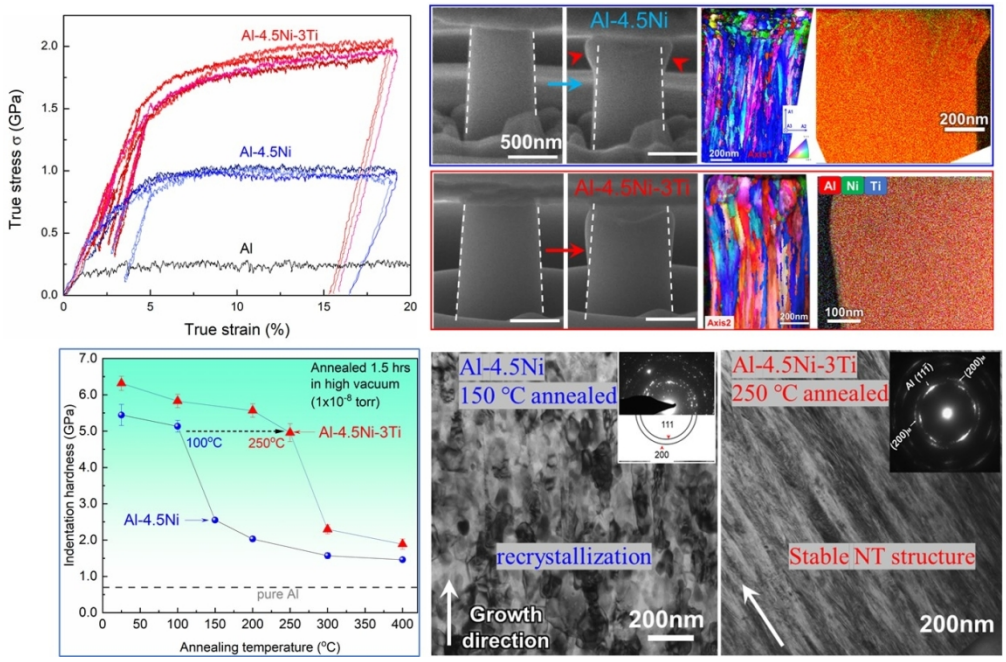

237x155mm (149 x 149 DPI)